Available online at www.CivileJournal.org

Civil Engineering Journal

(E-ISSN: 2476-3055; ISSN: 2676-6957)

Vol. 9, No. 01, January, 2023

Performance Comparison of Crossflow Turbine Configuration Upper Blade Convex and Curvature by Computational Method

Dendy Adanta [1*], Dewi Puspita Sari [2], Imam Syofii [2], Aji Putro Prakoso [3], Muhammad Amsal Ade Saputra [1], Ismail Thamrin [1]

[1] *Department of Mechanical Engineering, Faculty of Engineering, Universitas Sriwijaya, 30862, Sumatera, Indonesia.*

[2] *Study Program of Mechanical Engineering Education, Faculty of Education, Universitas Sriwijaya, 30862, Sumatera, Indonesia.*

[3] *Department of Mechanical Engineering, Faculty of Manufacturing Technology, Universitas Jenderal Ahmad Yani, West Java, Indonesia.*

Received 15 September 2022; Revised 04 December 2022; Accepted 12 December 2022; Published 01 January 2023

Abstract

A pico-hydro-type crossflow turbine (CFT) with an off-grid system configuration is a suitable option to increase the electrification ratio in remote or rural areas because it has a simple shape and can be applied in run-of-river conditions. Yet, a comprehensive study is necessary for the CFT to be applied to run-of-river conditions (low head and extreme fluctuation discharge), since this is categorized as an impulse turbine. One solution to optimize the CFT's performance in this context is to increase the lift force. Hence, this study investigated the effect of the upper blade of the CFT with convex and curved configurations using the computational fluid dynamics (CFD) method. The CFD transient approach uses a moving mesh feature, and the solver is pressure-based in low-head conditions (5 m pressure). The CFD results and analysis of variance (ANOVA) calculation results from this study reveal that the upper CFT affects the performance of the turbine. The relationship of the CFT performance with the rotation and specific speed is parabolic. The express empirical law relation for performance to rotation is a four-order polynomial, and for performance to a specific speed, a three-order polynomial. Based on empirical laws, a CFT with a convex blade is recommended for conditions with low head and extreme fluctuation discharge since it has a wider range of specific speeds than a curved blade, propeller, or Kaplan, Pelton, or Francis turbine.

Keywords: Computational Fluid Dynamics (CFD); Crossflow Turbine; Performance; Upper Blade; Specific Speed; Hydrodynamic.

1. Introduction

Electrification is an effective way to improve living standards [1], but remote areas are experiencing an electrical energy crisis. The pico-hydro-based off-grid-type crossflow turbine is a suitable option to increase the electrification ratio in remote areas. A crossflow turbine (CFT) is an economical turbine since it has a simple shape and can operate even when there are high flow-rate fluctuations (meaning it can be applied in run-of-river conditions) [2–5].

A CFT is an impulse-type turbine with medium-to-high head operating conditions. Yet, remote areas usually have run-of-river conditions, which are categorized as low-head. The energy conversion process has been studied by characterizing the CFT flow field as part of efforts to apply CFTs in low-head conditions. Several studies have shown that rotating flow often occurs in CFTs. Yet, this should be minimized since it causes hydraulic losses, consequently reducing a turbine's performance. The rotation often occurs between the blades in the middle of the runner [6]. Warjito et al. [7] studied the CFT flow field to determine the causes of losses in the nozzle and runner. Based on their results,

* Corresponding author: dendyadanta@ymail.com

http://dx.doi.org/10.28991/CEJ-2023-09-01-012

they proposed that the rear wall and 90° β_2 (blade angle at the outlet) can minimize the area prone to recirculation in the runner's centre. Then, Sammartano et al. [8] investigated the CFT energy conversion process and concluded that the CFT's performance is dominated by the blade shape (β_1 and β_2) and water velocity (C_1). Sammartano et al. [3] recommend 42° as the optimum blade angle in the inlet (β_1), and Chen and Choi [9] suggested 20° as the optimum angle of attack for C_1 (α_1).

There are three options for operating a CFT at a low head: design an inlet similar to a volute for parallel velocity vectors so that the momentum of the water to be transferred to each blade is proportional; increase the lift force, for instance, through the design of the CFT's upper blade; or optimize the ratio between the active and inactive blades. When we consider the first option, the nozzle geometry (incoming jet angle) is important to increase the discharge and the vector of the jet velocity [10]. An incoming jet angle (λ) of 50° was suggested in one study to indicate more profitable hydraulic behaviour than 60° to 90° [10]. Then, other studies recommended an λ of 60° after exploring a study range from 60° to 80° [11, 12]. All three studies cited [10–12] showed that the λ significantly affects the CFT performance and indicated the possibility that lower λ angles produce a better performance. In contrast, Anand et al. [13] hypothesized that a 90° λ should be used for the optimum efficiency; however, the authors failed to comprehensively explain the performance of each case in their report (which included a variation λ) [13]. Then, Piceno et al. [14] proposed a new nozzle design for CFTs; the inlet follows a convergence pipe concept, and the outlet uses a pressurized diffuser. The convergence pipe is combined with volute concepts to uniform the water velocity vector to the runner [14]. Based on numerical results, the maximum CFT performance when using the convergence pipe combined with volute concepts was 71.7% with a 90° λ [14], with 76% then offered in a follow-up study [15]. The two different results ($>\lambda >\eta$; $<\lambda >\eta$) reflect a difference in the nozzle design. The nozzle design should ensure all the velocity vectors of water hitting the blades are at their optimum, and C_1 should result in a 20° α_1. However, there is no conclusion yet on the optimum λ; extensive studies of λ are necessary to determine its optimal condition.

The second approach that may be applied to improve the CFT performance is to increase the lift force. To that end, this study focuses on the design of the CFT's upper blade. Curvature is the norm [16–18], following the lower geometry of the blade (Figure 1-a). Lift force occurs because of a difference in the flow fields between the upper and lower blades [19]. A previous study [20] showed that the concept of a CFT blade made from an aerofoil does not produce an increase in lift force because the blade tip becomes blunt and a taper is required. The blunt blade tip blocked the flow in a similar outcome to that found in another case study [21]. An appropriate alternative for increasing a CFT's lift force is to design the upper blade with a convex in the centre (Figure 1-b), where the flow field at the upper end is wider than that at the lower end. Accordingly, the water velocity in the upper blade is higher than that in the lower blade, creating a lift force. To test the approach, in this study, we investigated a CFT blade with a pointed tip and another with a convex-centre upper blade to determine the effect of lift force on the CFT's performance, which we assessed using the computational fluid dynamics (CFD) method. CFD allowed us to visualize flow phenomena in more detail than experiments would have enabled and thus gain a comprehensive understanding of the CFT energy conversion process; consequently, we determined which upper CFT blade configuration performed the best.

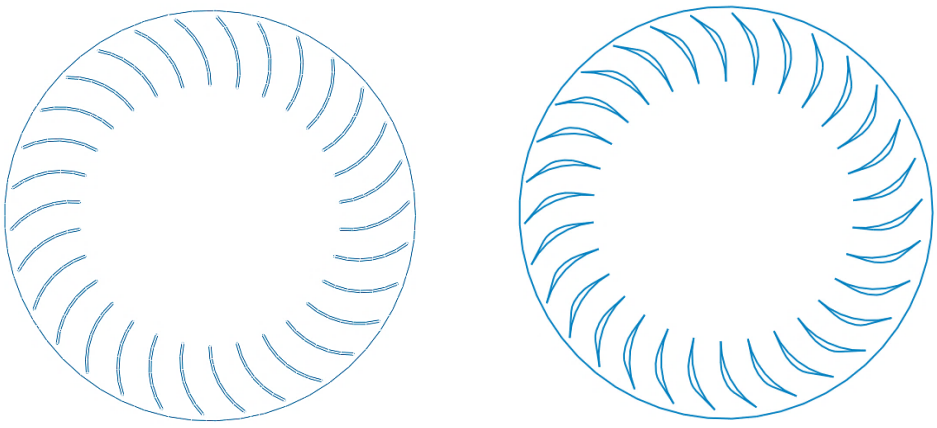

(a) (b)

Figure 1. Two-dimensional CFT runner: (a) Curved blade configuration; (b) Convex-at-centre blade configuration

2. Method

2.1. Geometry and Mechanical Power Analysis

Figure 2 presents the CFT's design; the lower blade design follows [22], and the nozzle design follows [18] enhanced by [10]. We employed analytical calculations using the study concept from [22] (validated by Adhikari and Wood [23]), with an optimum angle of attack (α_1) of 22°, blade angle at the inlet (β_1) of 40°, and blade angle at the outlet (β_2) of 90°. Moreover, the inner (D_{in}) and outer diameters of the runner (D_{out}) were taken as 18 and 11.78 cm, respectively. Another previous study [9] recommended using an optimum rear-wall angle (λ) of 50°.

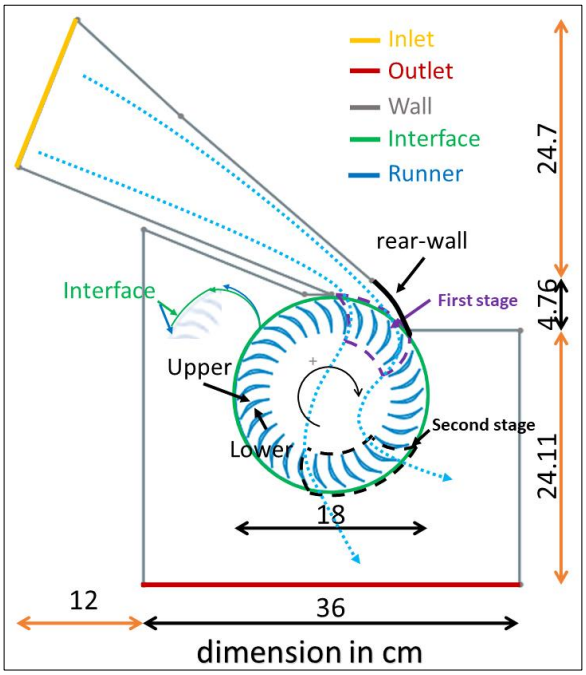

Figure 2. Two-dimensional CFT geometry

The mechanical power (P_{mech}) is the function of torque (τ) and angular velocity (ω), namely:

$$P_{\text{mech}} = \sum \tau \times \omega \tag{1}$$

Then, the performance of the turbine (η) is the function of P_{mech} and potential power (P_{avai}), namely:

$$\eta = \frac{P_{\text{mech}}}{P_{\text{avai}}} = \frac{\sum \tau \times \omega}{\rho \times g \times Q \times H} \tag{2}$$

where ρ is water density, g is gravity, Q is discharge, and H is the head. The specific speed (N_s) is a non-dimensional analysis used to determine whether the turbine is performing to its maximum in conditions Q and H. The N_s for a turbine is expressed using:

$$N_s = \frac{n \cdot {P_{\text{avai}}}^{0.5}}{\rho^{0.5} \cdot (g \cdot H)^{1.25}} \tag{3}$$

where n is the rotational speed of the runner.

2.2. CFD Method

The first equation for the simulation is continuity. The continuity equation [24] is given as follows:

$$\frac{\partial \rho}{\partial t} + \frac{\partial \rho u_j}{\partial x_j} = 0 \tag{4}$$

The next equation is the transport equation. For this, a momentum equation based on the Reynolds averaged Navier–Stokes (RANS) equation is required, with the body force (turbulence flow approach) and fluids flow categorized as Newtonian viscous fluids [24], so:

$$\frac{\partial \rho u_i}{\partial t} + \frac{\partial \rho u_i u_j}{\partial x_j} = -\frac{\partial \rho}{\partial x_i} + \frac{\partial}{\partial x_j}\left(\overline{\tau_{ij}} - \overline{\rho u_i' u_j'}\right) + \rho g_j \tag{5}$$

where p is pressure, τ_{ij} is the viscous stress tensor, $-\rho u_i' u_j'$ is the Reynolds stress tensor, and g is gravity. The modelling for $-\rho u_i' u_j'$ [25] is as follows:

$$-\overline{\rho u_i' u_j'} = \mu_t \left(\frac{\partial u_i}{\partial x_j} + \frac{\partial u_j}{\partial x_i}\right) - \frac{2}{3}\left(\rho k + \mu_t \frac{\partial u_i}{\partial x_i}\right)\delta_{ij} \tag{6}$$

where μ_t is the eddy (molecular) viscosity, k is the turbulence kinetic energy, and δ_{ij} is the Kronecker delta. Furthermore, the volume fraction (VoF) model is applied since the CFT operates at atmospheric pressure. The VoF model is:

$$\frac{\partial}{\partial t}(\alpha_n \rho_n) + \frac{\partial}{\partial x_j}(\alpha_n \rho_n u_{j,n}) = \frac{1}{V} \sum_{m=1}^{\text{all phase}} (\dot{m}_{mn} - \dot{m}_{nm}) \tag{7}$$

where ṁ is the mass transfer of the fluid phase, and the constant of interfacial surface tension is 0.0728 N·m [26].

The transition shear stress tensor (SST) can be applied to predict the turbulent flow in a CFT [27]. The SST model is an eddy viscosity model with two characteristics [24]. First, the numerical calculation for the fluid flow interaction in the inner boundary layer is made using the *k*-ω model for the outer region of the boundary layer, and using the *k*-ε model outside of it. Second, a limitation calculation is needed of the shear stress in regions with an adverse pressure gradient. The SST equations are as follows. For *k* [28, 29], the following equation is used:

$$\frac{\partial(\rho k)}{\partial t}+\frac{\partial\left(\rho k u_j\right)}{\partial x_j}=\frac{\partial}{\partial x_i}\left(\Gamma_k\frac{\partial k}{\partial x_j}\right)+G_k-Y_k+S_k \tag{8}$$

Then, for ω, this is the equation:

$$\frac{\partial(\rho \omega)}{\partial t}+\frac{\partial\left(\rho \omega u_j\right)}{\partial x_j}=\frac{\partial}{\partial x_i}\left(\Gamma_\omega\frac{\partial \omega}{\partial x_j}\right)+G_\omega-Y_\omega+S_\omega \tag{9}$$

where Γ_k and Γ_ω are the effective diffusivities, G_k and G_ω are the products of *k* and ω, Y_k and Y_ω are the dissipation of k and ω, and S_k and S_ω are user-defined source terms [28, 29].

Figure 3 presents the CFD simulation process. The wall, inlet, outlet, and interface are defined for boundary conditions. Then, the meshing process determines the number of the mesh using the grid convergence index (GCI) calculation. The simulation setup has eight steps. General section has three inputs: the solver is pressure-based, there is the transient approach, and gravity acts on the y-axis. The materials section required for the simulation are water and air. The model process has three inputs: VoF activation, a surface tension of 0.072 N/m, and a viscous model SST. The boundary condition process defines the inlet and outlet, both of which are as pressure. Then, defining the static and dynamic domains requires the determination of the mesh interface process.

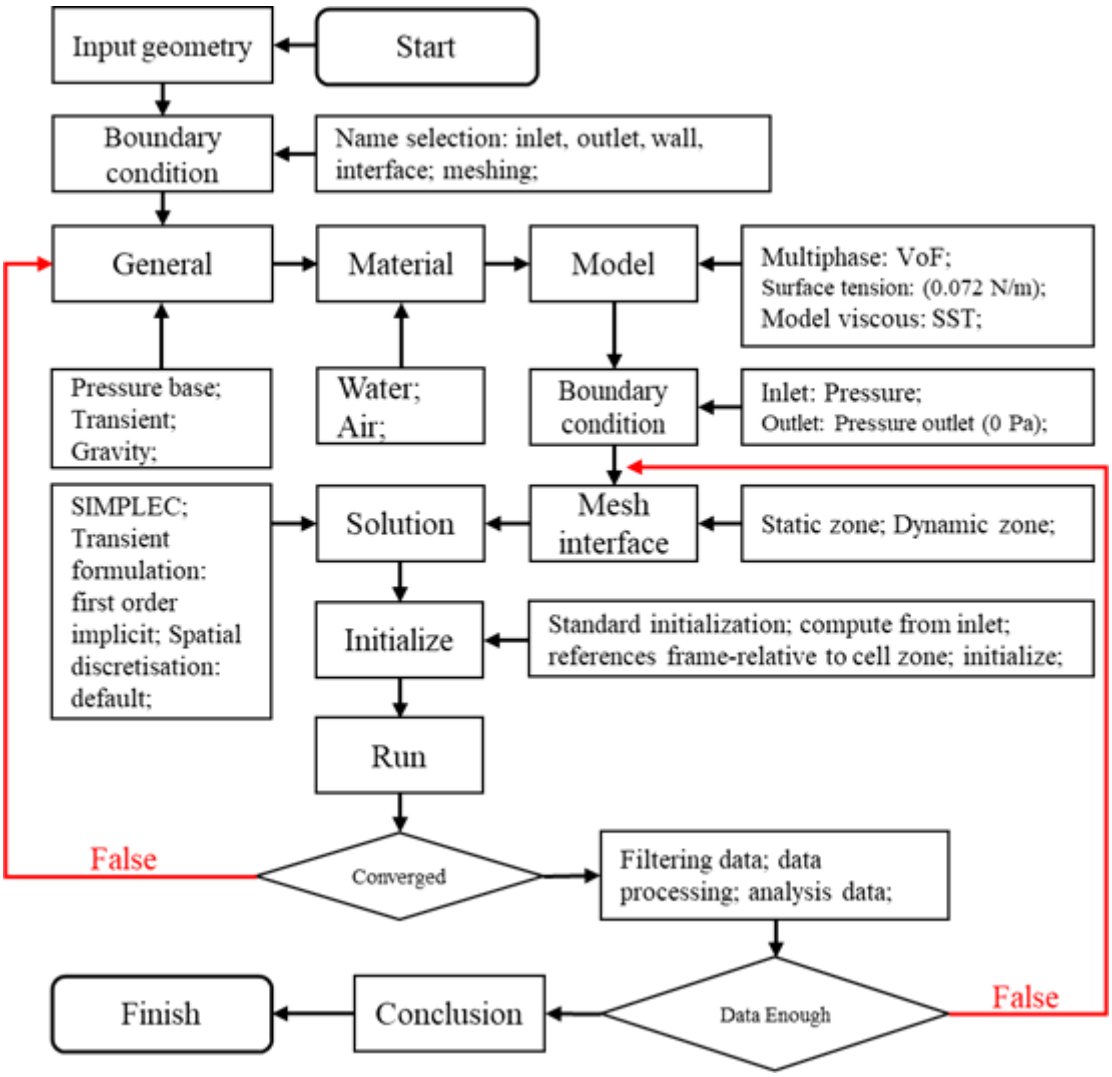

Figure 3. Flowchart of CFD simulation

Furthermore, the solution process has three setup steps: solution, transient formulation, and spatial discretization. SIMPLE is activated for the solution because the processing load is lighter than for SIMPLEC, SIMPLER, or PISO. The transient formulation is first-order implicit. Spatial discretization is the default. The solution has two setup conditions: the standard initialization must be computed from the inlet, and the reference frame must be relative to the cell zone. The setup of the reference frame for the water–liquid volume fraction is zero (0) since the initial condition at the inlet is assumed to be 100% water. Then, the simulation is run; if the numerical results do not converge, we revert to the general process. All data from the numerical results are filtered to minimize errors.

2.3. Independence Test Method

The parameters for the mesh test are based on the three vector calculation results (e.g. torque (τ)). The mesh test uses the GCI. Three mesh numbers (at least) are compared to determine the exact value ($\tau_{\to\infty}$). The calculation of $\tau_{\to\infty}$ using extrapolation concepts:

$$\tau_{\to\infty} = \tau_f - \left(\frac{\tau_m - \tau_f}{{b_{\text{fm}}}^{j_n+1} - 1}\right) \tag{10}$$

where b is the ratio of grid refinement. An example calculation is:

$$b_{\text{fm}} = \left(\frac{e_f}{e_m}\right)^{0.5} \tag{11}$$

where e is the element or mesh number. Then, f_{cm} is $2/b_{mc}$, f_{mf} is b_{mc}/b_{fm}, and f_{ff} is b_{fm}/b_{ff}. Moreover, j_n is obtained from numerical calculations, as follows:

$$j_{n+1} = ln\left|\left(\frac{\tau_c - \tau_m}{\tau_m - \tau_f}\left({b_{\text{fm}}}^{j_n-1}\right)\right) + {b_{\text{fm}}}^{j_n}\right| / ln(b_{\text{fm}} \times b_{\text{mc}}) \tag{12}$$

Usually, the initial number for j is 2. In that case, the GCI analysis becomes:

$$\text{GCI}_{\text{fm}} = S_f \left|\frac{1}{\tau_f}\frac{\tau_m - \tau_f}{{b_{\text{fm}}}^{j_n} - 1}\right| \times 100\% \tag{13}$$

where S_f is the safety factor of 1.25.

The timestep independency test uses the Courant number (C_o), a non-dimensional calculation of the fluid motion passing through an element or mesh. Ideally, the C_o is below 1; if it is more than that, this indicates that particles have gone uncalculated in the element or mesh (skip a cell) [26]. An example of the C_o calculation is given below:

$$C_o = u_i \times \frac{\Delta t}{\Delta x} \tag{14}$$

where Δx is the element or mesh size, Δt is the timestep, and u_i is the particle's average velocity.

3. Results and Discussion

3.1. Independence Test Results

Four mesh numbers were compared to determine which was optimal: 2.6k (2f), 10.7k (1f), 42.9k (0.5f), and 174.9k (0.25f). 0f is the exact value (that is, the $\tau_{\to\infty}$). Table 1 sets out the GCI calculation results. Based on Table 1, the 42.9k element or mesh number was suitable in this case, with an error of 3.03%, which showed it was appropriate since the recommended GCI percentage is below 5% [30]. Figure 4 offers a visualization of the 42.9k mesh or element number. Infiltration layer 4 is applied in this case to avoid calculation errors due to moving mesh; the implemented infiltration layer is applied to all blades.

Table 1. Independence test results for the element or mesh number

e	f	τ (N·m)	j_n	GCI (%)
2.6k	2	40.2		-
10.7k	1	44.1		11.04
42.9k	0.5	45.14	0.9938	3.03
174.9k	0.25	45.69		1.48
Continuum	0	45.91		

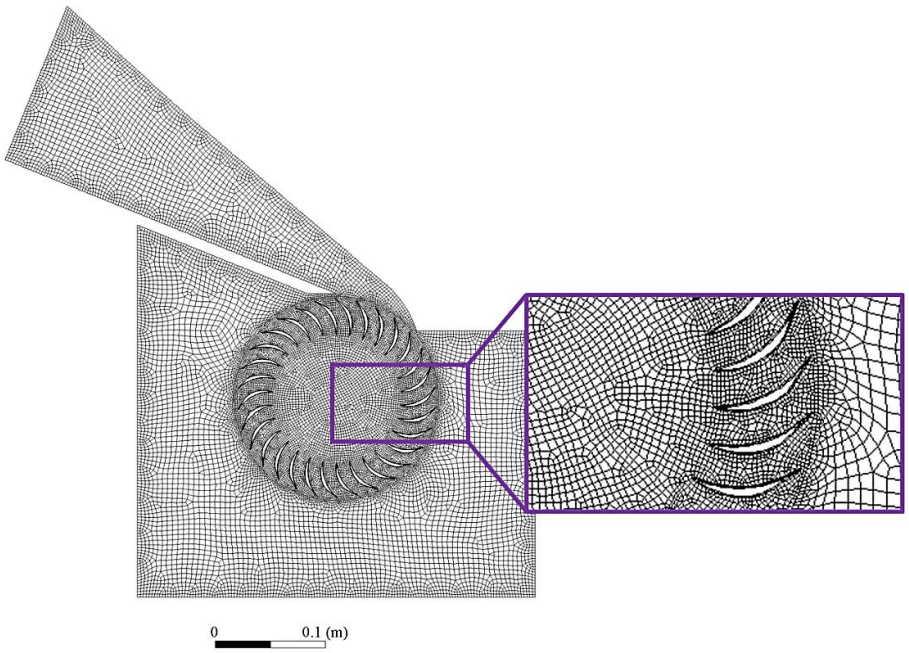

Figure 4. Mesh visualization for 42.9k

The 42.9k element or mesh number has a size (Δx) of 1.7 mm. Based on a probe, the average local velocity of water (u_i) was recorded as 3.1 m/s. Therefore, the recommended timestep size (Δt) based on suggestions from the literature ($C_o \leq 1$) was 0.0005s. Table 2 presents the C_o calculation results.

Table 2. Independence test results for the timestep size

Δx (mm)	u_i (m/s)	Δt (s)	C_o
1.7	3.1	0.00125	2.23
		0.0012	2.14
		0.0005	0.89
		0.0004	0.71

3.2. Computational Results

Figure 5 demonstrates the relationships of τ and P_{mech} with n (5-a: τ with n; 5-b P_{mech} with n). Based on Figure 5-a, the relationship of τ with n can be inferred to be linear, and can be expressed with:

$$\tau = a - b \cdot n \quad (15)$$

for convex blade a of 43.11 and b of 0.044, and for curved blade a of 33.74 and b of 0.03. The τ of the convex blade is higher than that of the curved blade for the n values of 400 and 500 rpm. Based on the estimation produced using Equation 15, the convex blades will have higher τ values than the curved blades at lower n values, and vice versa.

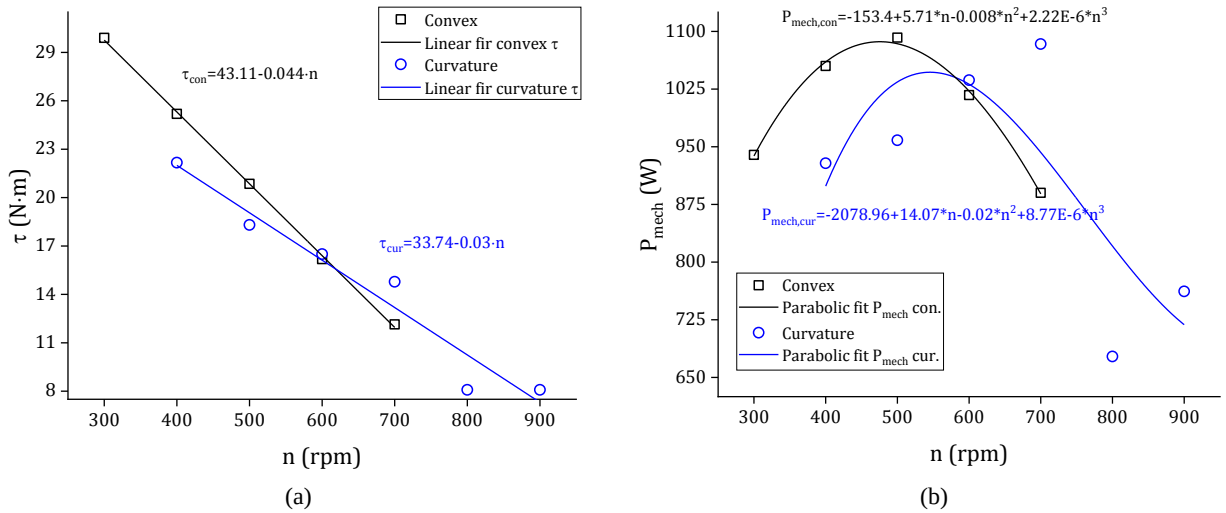

Figure 5. Relation of τ and P_{mech} to n

Then, based on Figure 5-b, the relationship of P_{mech} with n can be inferred to be parabolic, and can be expressed with:

$$P_{\text{mech}} = a + b \cdot n + c \cdot n^2 + d \cdot n^3 \quad (16)$$

for convex blade a of -153.4, b of 5.71, c of -0.008, and d of 2.22E-6, and for curved blade a of -2078.96, b of 14.07, c of -0.02, and d of 8.77E-6. Based on Figure 5-b, we can also determine that the P_{mech} for the convex blade is higher than that for the curved blade. For the convex blade, the highest P_{mech} is 1091.92 W at 500 rpm, while for the curved blade, this is 1083.57 W at 600 rpm.

Figure 6 reveals the relationships of η with n and N_s (6-a: η with n; 6-b: η with N_s). Based on Figure 6, these can be determined to be parabolic. The relationship of η with n can be expressed as:

$$\eta = a + b \cdot n + c \cdot n^2 + d \cdot n^3 + e \cdot n^4 \quad (17)$$

for convex blade a of -2.4, b of 5.71, c of 0.326, d of 3.66E-4, and e of 5.84E-8, and for curved blade a of -39.34, b of 5.71, c of 0.39, d of 3.47E-4, and e of 1.52E-8. In Figure 6-a, we can see that the curved blade has a better performance (76.94%) than the convex blade (76.84%). Compared to a previous study [10], the CFT upper blade geometry (convex and curvature) changes went further to improve its performance, from a 61% [10] improvement to 76.84% (convex blade) or 76.94% (curved blade). Yet, the relationship of η with n is similar to in the previous study [18, 23], which verifies the simulation results.

$$\eta = a + b \cdot N_s + c \cdot {N_s}^2 + d \cdot {N_s}^3 \quad (18)$$

for convex blade a of 3.65, b of 29.36, c of -2.52, and d of -0.09, and for curved blade a of -53.84, b of 48.09, c of -4.54, and d of -0.004. Based on the prediction made using Equation 18, for a performance over 65%, the N_s range for the convex blade is more profitable, at 3.51 (from 2.87 to 6.38), than that for the curved blade, at 2.85 (from 3.91 to 6.76).

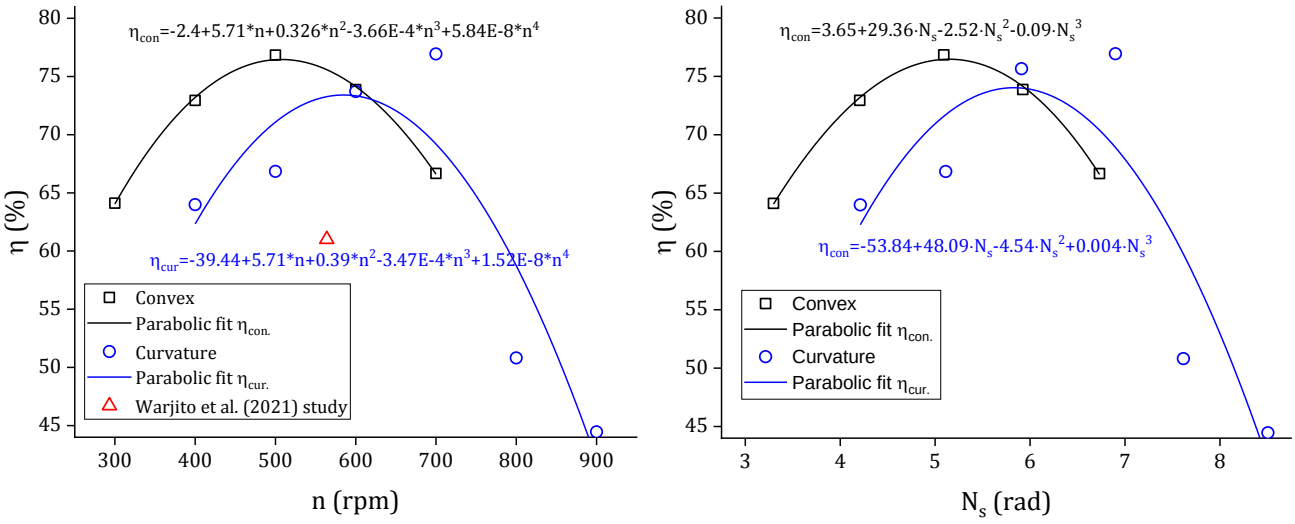

(a) (b)

Figure 6. Relationship of η with n and N_s

3.3. Discussion

Figure 7 visualizes the velocity contours (7-a convex blade; 7-b curved blade). In Figure 7-a, the first and second stages indicate the lift force produced, where the water velocity in the upper blade is higher than that in the lower blade. In contrast (Figure 7-b), for the curved blade, there is no significant difference in water velocity between the upper and lower parts of the blade. Figure 7-a demonstrates that the lift force does not significantly contribute to the P_{mech} produced by the runner with the curved blade, similar to the finding of a previous study [20]. Meanwhile, insignificant lift force is created by the linear curved blade shown in Figure 7-b, where, in the second stage, the water velocity in the lower blade is higher than that in the upper blade; indeed, this configuration was not good for the CFT.

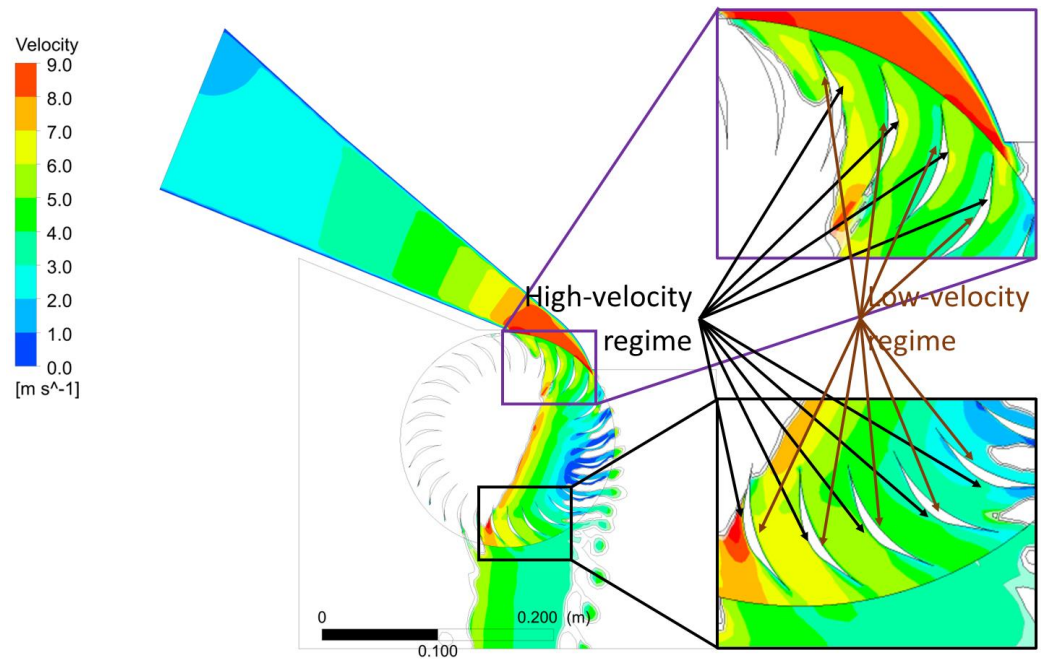

(a)

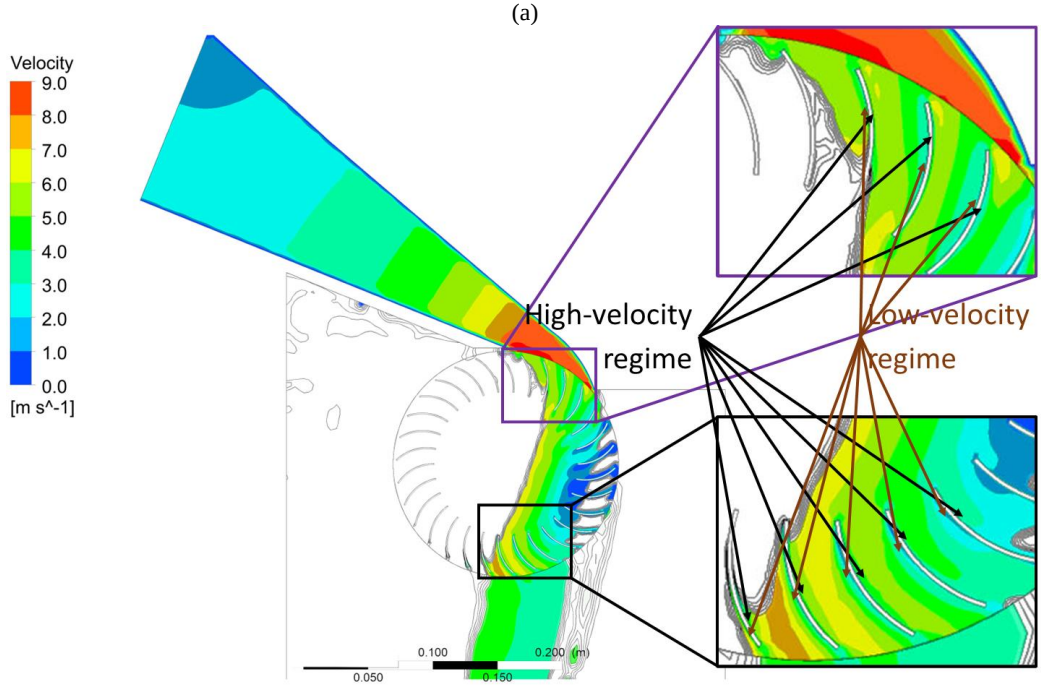

(b)

Figure 7. Visualization of the velocity of water

From Figure 6-b, we can surmise that a CFT is less desirable than a Kaplan, Pelton, or Francis turbine since it has lower off-design efficiency. A Kaplan or propeller turbine is the preferred option even for low-to-medium-head conditions with medium or low discharge (Q) (run of river). The CFT has low efficiency but has a wider N_s range, from 2.87 to 6.38 rad, than the Kaplan, Pelton, and Francis turbines (Kaplan turbine, 1.55–4.5 rad; Pelton turbine, 0.1–0.5 rad; Francis turbine, 0.26–2.45 rad [31]). The N_s range for the convex and curved blades in Figure 5-b is similar to Mockmore and Merryfield's [32] finding of 4.4 rad (275 rpm) and Warjito et al.'s [10] finding of 3 rad. The advantage of a wide N_s range is that the turbine can work optimally despite extreme fluctuations in head and discharge (see Equation 2).

In addition, the energy conversion ratio in the first and second stages is similar to that recommended by Andrade et al. [6], with a first stage ±70% and second stage ± 0% (Figure 8). As can be seen from Figure 8, the energy conversion on the convex blade is higher than on the curved blade; this condition is in line with the ANOVA results, which show the blade shape affects the CFT's performance. Furthermore, based on Figure 9, the active blade for convex blade of 11 is better than that of curved blade of 10. Therefore, Table 3 and Figure 8 indicate that taking this approach to improve the efficacy of a CFT can be recommended when using a convex blade.

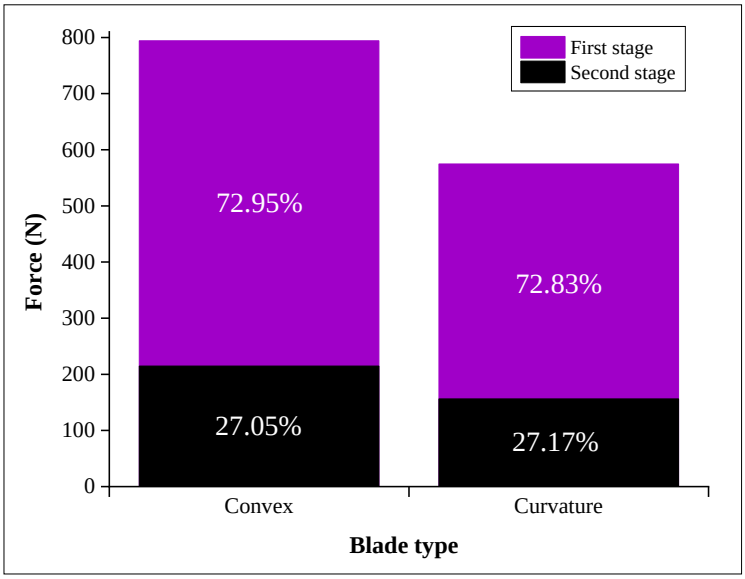

Figure 8. Proportions of energy conversion in the first and second stages at peak performance

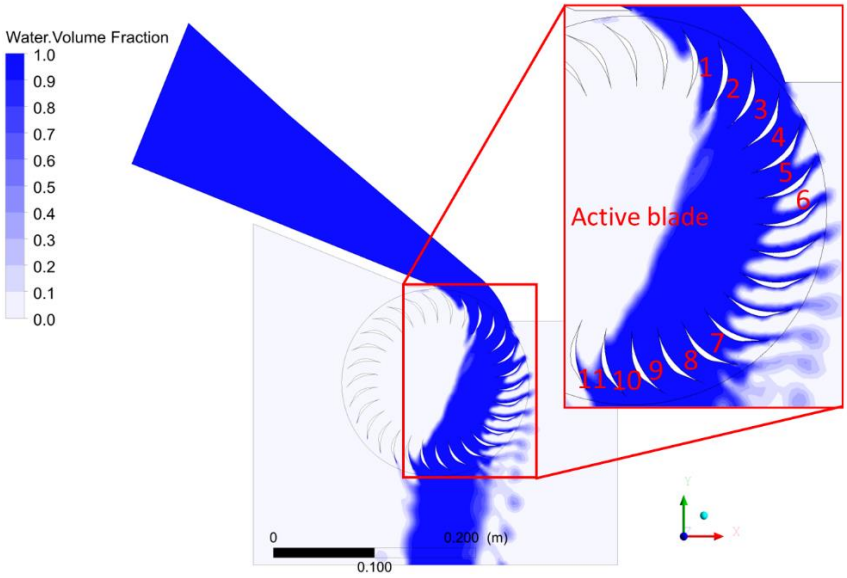

(a)

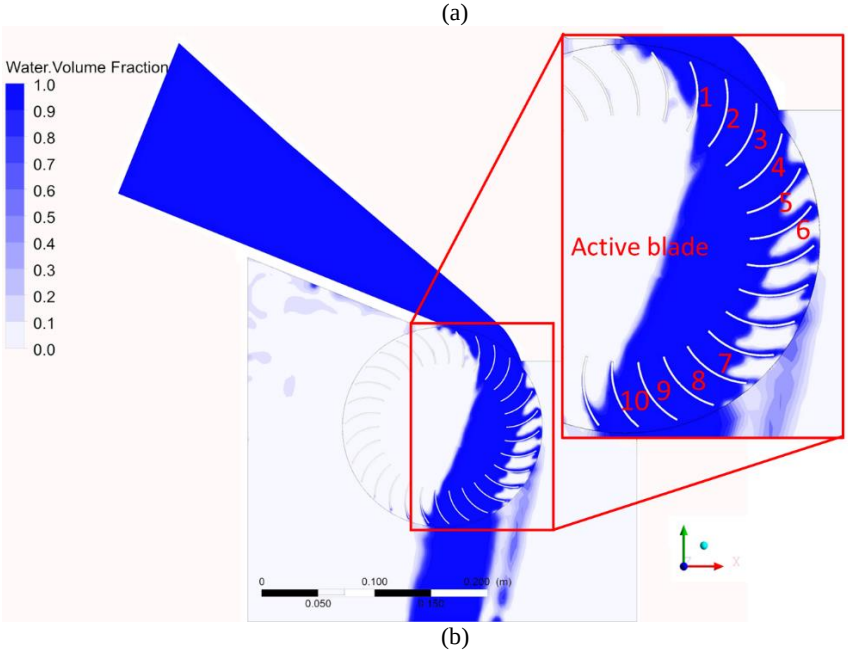

(b)

Figure 9. Visualization of water volume fraction

Table 3. Single factor ANOVA

Source	Sum of square	DF	Mean square	F	P_{-value}	F_{crit}
Upper blade configuration	49.86	1	49.86	6.6	0.017	4.28
Error	173.65	23	7.55			
Total	405.27	47				

From Figure 9, the hypothesis about the effect of the active-to-inactive blade ratio in CFTs can be said to be verified. The curved blade has a lower active-to-inactive blade ratio than the convex blade. As a result, water is trapped in the inactive blade between active blade numbers 6 and 7 (at the inlet's second stage). The water that is trapped is considered a loss since it inhibits the runner's rotation and torque. The trapped water reduces the force (torque) of the curved blade, which explains why that is lower than the force of the convex blade (Figure 8).

Figure 10 illustrates the pressure contours of the water phase. In Figure 10, low pressure on the upper convex blade is wider than the curved blade. The low pressure on the upper blade also indicates a contribution made by lift force to the CFT energy conversion process. The wider the low pressure on the upper blade, the greater the positive impact. Figure 10 aligns with Figures 5, 6, and 8, in which a wider blade with lower pressure generates greater τ and, consequently, the P_{mech} and η increase. Based on Figure 10, we propose that lift force can be generated and increased in the CFT by designing its blade with a convex configuration.

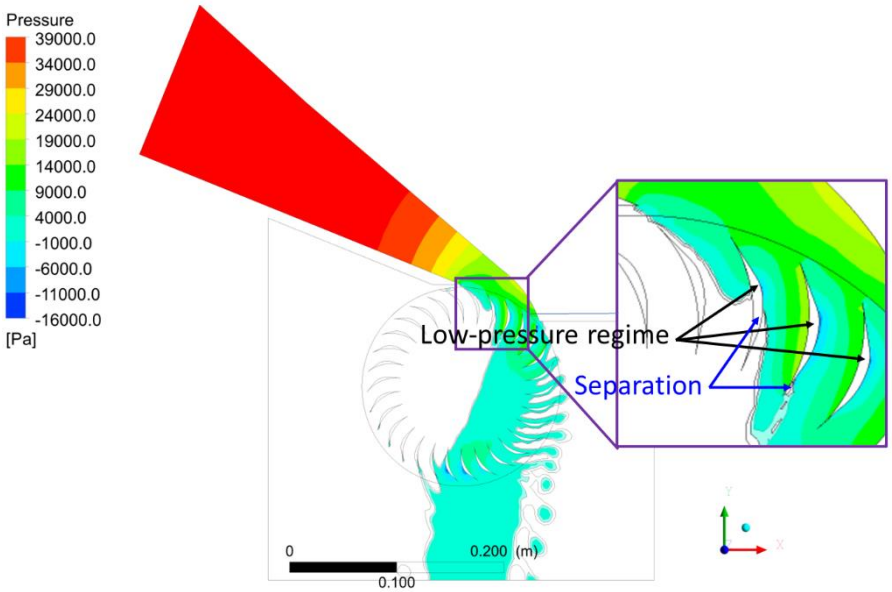

(a)

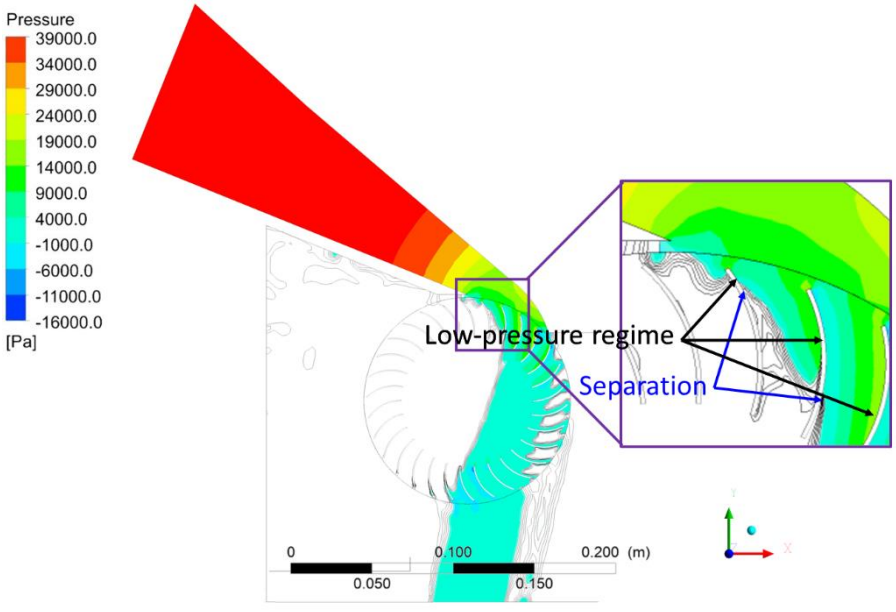

(b)

Figure 10. Visualization of pressure contour

4. Conclusion

A pico-hydro-type crossflow turbine (CFT) with an off-grid system configuration is a suitable option to increase the electrification ratio in remote or rural areas. A CFT is an economical turbine since it has a simple shape and can operate with high flow-rate fluctuations, meaning it can be operated in run-of-river conditions [2–4]. However, a CFT is impulse-categorized, so comprehensive studies are necessary before it can be applied to run-of-river conditions (low head and extreme fluctuation discharge). In that context, one solution to increasing the CFT's performance is to increase the lift force. Therefore, this work investigated the performance of CFT upper blades with convex and curved configurations. The CFD method based on the feature moving mesh approach was taken to determine the performance of the two blade configurations with variations in the runner rotation. A pressure-based solver was used given the incompressible fluid flow and the inlet boundary condition pressure of 5 m (low head). Based on our CFD results and ANOVA analysis, we can surmise that the upper CFT affects its performance. The relationships of the performance of the CFT with the rotation and specific speed are parabolic; for the performance and rotation, this constitutes four-order polynomials, and for the performance and specific speed, three-order polynomials. The curved blade achieved the highest performance of 76.94%, and the convex blade achieved the highest performance of 76.84%. When we studied the specific speed, the range for the convex blade was 2.87–6.38 rad, and that for the curved blade was 3.91–6.76 rad, meaning the convex blade is more productive than the curved blade. Based on the specific speed range, the CFT with the convex blade is recommended for low-head and extreme fluctuation discharge conditions since it has a wider range of specific speed than the curved blade, propeller, or Kaplan, Pelton, or Francis turbines. This leads us to conclude that the CFT turbine is a low-cost generating solution that can be applied in run-of-river conditions.

5. Declarations

5.1. Author Contributions

Conceptualization, D.A. and A.P.P.; methodology, I.S. and D.P.S.; software, M.A.A.S.; validation, I.T., D.A. and A.P.P.; formal analysis, D.A.; investigation, IS; resources, D.P.S.; data curation, I.T.; writing—original draft preparation, D.A.; writing—review and editing, D.P.S. and I.S.; visualization, M.A.A.S.; supervision, A.P.P.; project administration, D.P.S.; funding acquisition, D.A. All authors have read and agreed to the published version of the manuscript.

5.2. Data Availability Statement

The data presented in this study are available in the article.

5.3. Funding and Acknowledgments

This research was supported by Directorate of Research, Technology and Community Service (DRTPM) and Directorate General of Higher Education, Research, and Technology (DIRJENDIKTI) with grant number: 142/E5/PG.02.00.PT/2022.

5.4. Conflicts of Interest

The authors declare no conflict of interest.

6. References

[1] Adanta, D. B. W., Quaranta, E., & I. Mahlia, T. M. (2019). Investigation of the effect of gaps between the blades of open flume Pico hydro turbine runners. Journal of Mechanical Engineering and Sciences, 13(3), 5493–5512. doi:10.15282/jmes.13.3.2019.18.0444.

[2] Montanari, R. (2003). Criteria for the economic planning of a low power hydroelectric plant. Renewable Energy, 28(13), 2129–2145. doi:10.1016/S0960-1481(03)00063-6.

[3] Sammartano, V., Morreale, G., Sinagra, M., & Tucciarelli, T. (2016). Numerical and experimental investigation of a cross-flow water turbine. Journal of Hydraulic Research, 54(3), 321–331. doi:10.1080/00221686.2016.1147500.

[4] Sinagra, M., Sammartano, V., Aricò, C., Collura, A., & Tucciarelli, T. (2014). Cross-Flow turbine design for variable operating conditions. Procedia Engineering, 70, 1539–1548. doi:10.1016/j.proeng.2014.02.170.

[5] Achebe, C. H., Okafor, O. C., & Obika, E. N. (2020). Design and implementation of a crossflow turbine for Pico hydropower electricity generation. Heliyon, 6(7), 4523. doi:10.1016/j.heliyon.2020.e04523.

[6] De Andrade, J., Curiel, C., Kenyery, F., Aguilln, O., Vásquez, A., & Asuaje, M. (2011). Numerical investigation of the internal flow in a Banki turbine. International Journal of Rotating Machinery, 2011. doi:10.1155/2011/841214.

[7] Warjito, W., Budiarso, B. & Adanta, D. (2021). Computational analysis of flow field on cross-flow hydro turbines. Engineering Letters, 29(1), 87–94.

[8] Sammartano, V., Aricò, C., Carravetta, A., Fecarotta, O., & Tucciarelli, T. (2013). Banki-Michell optimal design by computational fluid dynamics testing and hydrodynamic analysis. Energies, 6(5), 2362–2385. doi:10.3390/en6052362.

[9] Choi, Y.-D., Lim, J.-I., Kim, Y.-T., & Lee, Y.-H. (2008). Performance and Internal Flow Characteristics of a Cross-Flow Hydro Turbine by the Shapes of Nozzle and Runner Blade. Journal of Fluid Science and Technology, 3(3), 398–409. doi:10.1299/jfst.3.398.

[10] Warjito, W., Budiarso, B., Celine, K., & Nasution, S. B. S. (2021). Computational Method for Designing a Nozzle Shape to Improve the Performance of Pico-Hydro Crossflow Turbines. International Journal of Technology, 12(1), 139. doi:10.14716/ijtech.v12i1.4225.

[11] Aliman, I., Kurniawati, I., Wulandari, J. A., & Sutikno, P. (2018). Evaluation design and simulation of three-way nozzle and control flow vane nozzle on cross flow water turbine for various head. AIP Conference Proceedings. doi:10.1063/1.5046631.

[12] Sutikno, P., Seyhak, D., Diasta, I. N., Firmansyah, I., & Zulkarnain. (2017). Investigation of the Standardized a Cross Flow Turbine Used the Numerical Simulation and Experimental Results. Proceedings of the 14th Asian International Conference on Fluid Machinery, 10-13 November, 2017, Jiangsu, China.

[13] Anand, R. S., Jawahar, C. P., Bellos, E., & Malmquist, A. (2021). A comprehensive review on Crossflow turbine for hydropower applications. Ocean Engineering, 240, 110015. doi:10.1016/j.oceaneng.2021.110015.

[14] Picone, C., Sinagra, M., Aricò, C., & Tucciarelli, T. (2021). Numerical analysis of a new cross-flow type hydraulic turbine for high head and low flow rate. Engineering Applications of Computational Fluid Mechanics, 15(1), 1491–1507. doi:10.1080/19942060.2021.1974559.

[15] Hannachi, M., Ketata, A., Sinagra, M., Aricò, C., Tucciarelli, T., & Driss, Z. (2021). A novel pressure regulation system based on Banki hydro turbine for energy recovery under in-range and out-range discharge conditions. Energy Conversion and Management, 243, 114417. doi:10.1016/j.enconman.2021.114417.

[16] Adhikari, R. (2016). Design improvement of crossflow hydro turbine. Ph.D. Thesis, University of Calgary, Calgary, Canada. doi:10.11575/PRISM/25581.

[17] Adhikari, R. C., & Wood, D. H. (2018). Computational analysis of part-load flow control for crossflow hydro-turbines. Energy for Sustainable Development, 45, 38–45. doi:10.1016/j.esd.2018.04.003.

[18] Sinagra, M., Sammartano, V., Aricò, C., & Collura, A. (2016). Experimental and Numerical Analysis of a Cross-Flow Turbine. Journal of Hydraulic Engineering, 142(1), 04015040–1–04015040–8,. doi:10.1061/(asce)hy.1943-7900.0001061.

[19] Munson, B. R., Young, D. F., & Okiishi, T. H. (1994). Fundamentals of fluid mechanics. Wiley, Hoboken, United States. doi:10.1201/b11709-7.

[20] Adanta, D., Budiarso, Warjito, Siswantara, A. I., & Prakoso, A. P. (2018). Performance comparison of NACA 6509 and 6712 on pico hydro type cross-flow turbine by numerical method. Journal of Advanced Research in Fluid Mechanics and Thermal Sciences, 45(1), 116–127.

[21] Zaffar, A., Ibrahim, B., Sarwar, M. A., Chattha, J. A., & Asif, M. (2018). Optimization of blade profiles of cross flow turbine. International Journal of Power and Energy Conversion, 9(4), 311–326. doi:10.1504/IJPEC.2018.094952.

[22] Adanta, D. (2020). Investigation of the Constant of Bachelor and Kolmogorov on Standard k-epsilon Turbulence Model for Cross-Flow Pico-Hydro Turbine. PhD Thesis, Universitas Indonesia, Depok City, Indonesia. (In Indonesian).

[23] Adhikari, R., & Wood, D. (2018). The design of high efficiency crossflow hydro turbines: A review and extension. Energies, 11(2), 1–18,. doi:10.3390/en11020267.

[24] Davidson, L. (2018). Fluid mechanics, turbulent flow and turbulence modeling. Chalmers University of Technology, Goteborg, Sweden.

[25] Tennekes, H., & Lumley, J. L. (2020). A First Course in Turbulence. MIT Press, Cambridge, Massachusetts, United States. doi:10.7551/mitpress/3014.001.0001.

[26] ANSYS Fluent. (2013). Release 15.0, Theory Guide. Pennsylvania, United States.

[27] Siswantara, A. I., Budiarso, Prakoso, A. P., Gunadi, G. G. R., Warjito, & Adanta, D. (2018). Assessment of turbulence model for cross-flow pico hydro turbine numerical simulation. CFD Letters, 10(2), 38–48.

[28] Menter, F. (1993). Zonal Two Equation k-w Turbulence Models for Aerodynamic Flows. 23rd Fluid Dynamics, Plasma dynamics, and Lasers Conference. doi:10.2514/6.1993-2906.

[29] Menter, F. R. (1994). Two-equation eddy-viscosity turbulence models for engineering applications. AIAA Journal, 32(8), 1598–1605. doi:10.2514/3.12149.

[30] Roache, P. J. (1998). Verification and validation in computational science and engineering. Hermosa, New Mexico, United States.

[31] Ingram, G. (2009). Basic concepts in turbomachinery. Bookboon, London, United Kingdom.

[32] Mockmore, C. A., & Merryfield, F. (1949). The Banki water turbine. Bulletin Series No. 25, Oregon State University, Corvallis, United States.